Phononic Thermal Transport along Graphene Grain Boundaries: A Hidden Vulnerability

Zhen Tong, Alessandro Pecchia, ChiYung Yam, Traian Dumitrică,* and Thomas Frauenheim*

While graphene grain boundaries (GBs) are well characterized experimentally, their influence on transport properties is less understood. As revealed here, phononic thermal transport is vulnerable to GBs even when they are ultra-narrow and aligned along the temperature gradient direction. Non-equilibrium molecular dynamics simulations uncover large reductions in the phononic thermal conductivity (κ_p) along linear GBs comprising periodically repeating pentagon-heptagon dislocations. Green's function calculations and spectral energy density analysis indicate that the origin of the κ_p reduction is hidden in the periodic GB strain field, which behaves as a reflective diffraction grating with either diffuse or specular phonon reflections, and represents a source of anharmonic phonon–phonon scattering. The non-monotonic dependence with dislocation density of κ_p uncovered here is unaccounted for by the classical Klemens theory. It can help identify GB structures that can best preserve the integrity of the phononic transport.

1. Introduction

The next generation of high-performance electronics and sensors require materials with high thermal conductivity (κ_p) able to spread effectively the high density of Joule heat generation along and across various thin films and substrates.[1,2] 2D materials including graphene are very attractive[3,4] for these applications as they are relatively immune to detrimental size effects on basal-plane thermal conductivity. This is because the highly anisotropic phonon group velocity reduces the impact of scattering by the top and bottom surfaces.[5,6] Nevertheless, thermal transport is significantly impacted[7] by defects formed during synthesis. In this respect, the widely used chemical vapor deposition (CVD)[8] unavoidably produces grain boundaries (GBs). As domains nucleate randomly on substrates, their CVD growth and coalescence result in the formation of GBs.[9–12]

GBs are imagined as periodic arrays of dislocations.[13] In graphene, GBs are strings of pentagon-heptagon (5-7) edge dislocations[10,14–16] and their organization can gives rise to diverse GB shapes. While in general the thermal gradient can have an arbitrary orientation with respect to the GB line,[17,18] only transport across GBs is perceived to have a significantly impact on heat transport. Green's function (GF) calculations[19,20] obtained that heat transmission across GBs can be influenced by the GB structure, size, and shape. Non-equilibrium molecular dynamics (NEMD) simulations[21–23] revealed a discontinuity in the temperature (T) profile across GBs and that higher dislocation densities lead to lower κ_p.

In this work, we reveal that, in fact, thermal transport is not immune to GBs oriented along the thermal gradient. By way of NEMD simulations with LAMMPS,[24] we report κ_p reduction along GBs with various 5-7 dislocation densities and length scales L between 10 to 1000 nm, in systems of up to 590 512 carbon (C) atoms treated with the optimized Tersoff potential.[25] To gain a clear understanding, we further conducted GF calculations of phononic transmission and conductance, and spectral energy density (SED) calculations to quantify phonon relaxation times. The κ_p uncovered by these calculations displays a subtle, non-monotonic dependence on 5-7 defect density which is unaccounted for by the classical theory of Klemens.[7]

2. Results and Discussion

The NEMD setup is presented in **Figure 1**a. Two-unit cells at each end were kept fixed throughout simulation and ten other

Dr. Z. Tong, Prof. C. Yam, Prof. T. Frauenheim
Shenzhen JL Computational Science and Applied Research Institute
Shenzhen 518131, China
E-mail: thomas.frauenheim@bccms.uni-bremen.de

Dr. A. Pecchia
CNR-ISMN
Via Salaria km 29.300, Monterotondo, Rome 00017, Italy

Prof. C. Yam, Prof. T. Frauenheim
Beijing Computational Science Research Center
Beijing 100193, China

Prof. T. Dumitrică
Department of Mechanical Engineering
University of Minnesota
Minneapolis, MN 55455, USA
E-mail: dtraian@umn.edu

Prof. T. Frauenheim
Bremen Center for Computational Materials Science
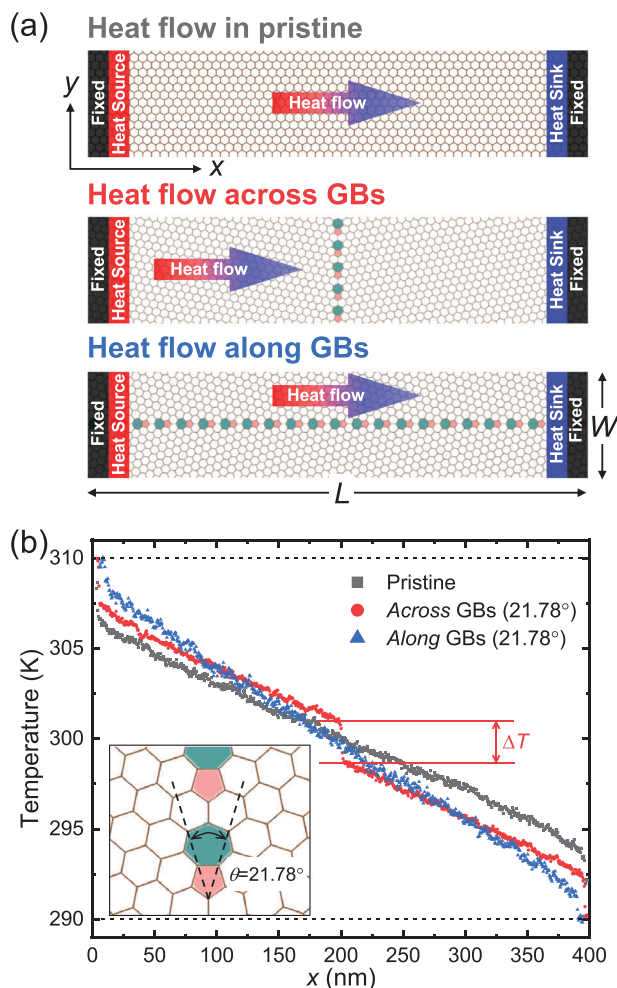University of Bremen
Bremen 2835, Germany

Figure 1. a) NEMD setup for pristine and GB graphene with $\theta = 21.78°$. PBC are imposed along y. b) Computed T profiles.

neighboring unit cells were designated as "hot" and "cold" baths maintained at the temperatures $T_h = 310$ K and $T_c = 290$ K, respectively. At steady-state, the heat flux $\dot{Q}$ was calculated as the difference of the rate of the kinetic energy extraction from the two reservoirs $\dot{Q} = 0.5\langle \dot{Q}_h - \dot{Q}_c \rangle$, where $\dot{Q}_h$ and $\dot{Q}_c$ are the instantaneous heat currents flowing into and away from the "hot" and "cold" baths. The angular brackets indicate a statistical average taken after the steady state was reached. Graphene edges[26] can significantly impact thermal transport.[17] The application of periodic boundary conditions (PBC) along y eliminates lateral edges and allows for the simulation of the thermal transport perpendicular to a single GB line and along antiparallel GB lines (i.e, the 5-7 defect lines run parallel to each other but with opposite directionality) separated by the lateral periodicity W. Therefore, differences in calculated T profiles, Figure 1b, can be attributed solely to GBs.

The NEMD calculations of Figure 1b at $L = 400$ nm and $W = 15.5$ nm reveal a stark difference between the T profiles across and along the considered GBs, which comprises aligned 5-7 defects separated by one hexagonal ring. In agreement with Azizi et al.,[23] we see a sharp temperature drop $\Delta T = 2.2$ K, corre-

sponding to a thermal resistance $\Delta T/\dot{q}$ of 0.035 Km^2/GW across this GB. Here $\dot{q}$ is $\dot{Q}$ per cross-sectional area (defined here based on the 0.33 nm thickness of graphene[21]). Along the GB line, the T profile is smooth and resembles the one obtained for the pristine graphene. By thermal symmetry, the GB lines oriented along the heat flow are adiabatic lines. If heat transfer was purely 1D, then κ_p would be hardly changed. However, the extracted $\kappa_p = -\dot{q}(dT/dx)^{-1}$, reveal a $\approx 50\%$ reduction (633.2 ± 2.5 W mK^{-1} versus 1259.4 ± 7.5 W mK^{-1}) demonstrating that through the two-dimensionality of the heat transport, κ_p is significantly impacted even by such linear ultra-narrow GBs.

We have checked the robustness of our result (see Figure S2, Supporting Information) on a collection of symmetric tilt GB structures with similar widths W but different L and spread out linear arrangements of the 5-7 defects, which decrease the tilt angles θ[27] formed by the crystallographic directions of the neighboring domains, **Figure 2**a. It is important to note that each 5-7 defect introduces local off-plane elevations[28] as a way of reliving the strain stored in the dislocation core. The resulting "bumpy" landscape with a rather blazed profile is visible in Figure 2b for the $\theta = 4.41°$ GB. The off-plane displacements are opposite in neighboring GB lines, such that stable ripple structures are formed. As shown in the side views of Figure 2a, the ripples acquire significant amplitudes of 15±1.5Å. Only for $\theta = 21.78°$, the closeness of the 5-7 cores inhibits their off-plane displacements reducing the ripple amplitude to only 4.17 Å. For this case, the C–C bond deformations are continuous along the GB line, Figure 2b. On the same figure, it can be also seen that the C–C bond extension and compression deformations are strongly localized around the 5-7 cores. Overall, in all of the rippled structures of Figure 2, the C–C bond extension and compression deformations are strongly localized around the 5-7 cores. The axial prestrain is also very small; it varies monotonically with θ, from -0.2% ($\theta = 4.41°$) to 0.1% ($\theta = 21.78°$), see Figure S1b, Supporting Information.

Figure 3a demonstrates that the differences between κ_p in pristine ($\theta = 0°$)[29,30] and along GBs with different θ remain significant at different L. In the pristine case, the initial linear increase of κ_p, a signature of ballistic transport,[30] changes (at $L \approx 80$ nm) into a logarithmic dependence, which is expected to hold at L much larger than the average phonon mean free path (≈ 775 nm at $T = 300$ K).[29,30] The unusual $\approx \log L$ scaling originates in the combination of reduced dimensionality of the system and the excessive population of out-of-plane modes.[30] Along GBs, the $\kappa_p \approx \log L$ dependence is significantly attenuated such that the departure from the pristine case increases with L. At the largest considered $L = 1,000$ nm, the κ_p reduction is $\approx 60\%$ or larger with respect to the pristine case. Furthermore, the κ_p dependence on the dislocation density is anomalous: While the dislocation density increases with θ, κ_p displays non-monotonic variations, which become more pronounced for $L > 100$ nm, Figure 3b. κ_p decreases from $\theta = 4.41°$ up to $\theta = 13.18°$ but presents an anomalous enhancement at $\theta = 21.78°$, where the 5-7 density is the largest.

What is the mechanism responsible for the surprising anomalous κ_p reduction along GBs? To answer this question we first focus on the initial ballistic regime, where we have carried out complementary GF investigations. As in NEMD, we partitioned the system into "hot" bath, device region, and "cold" bath,
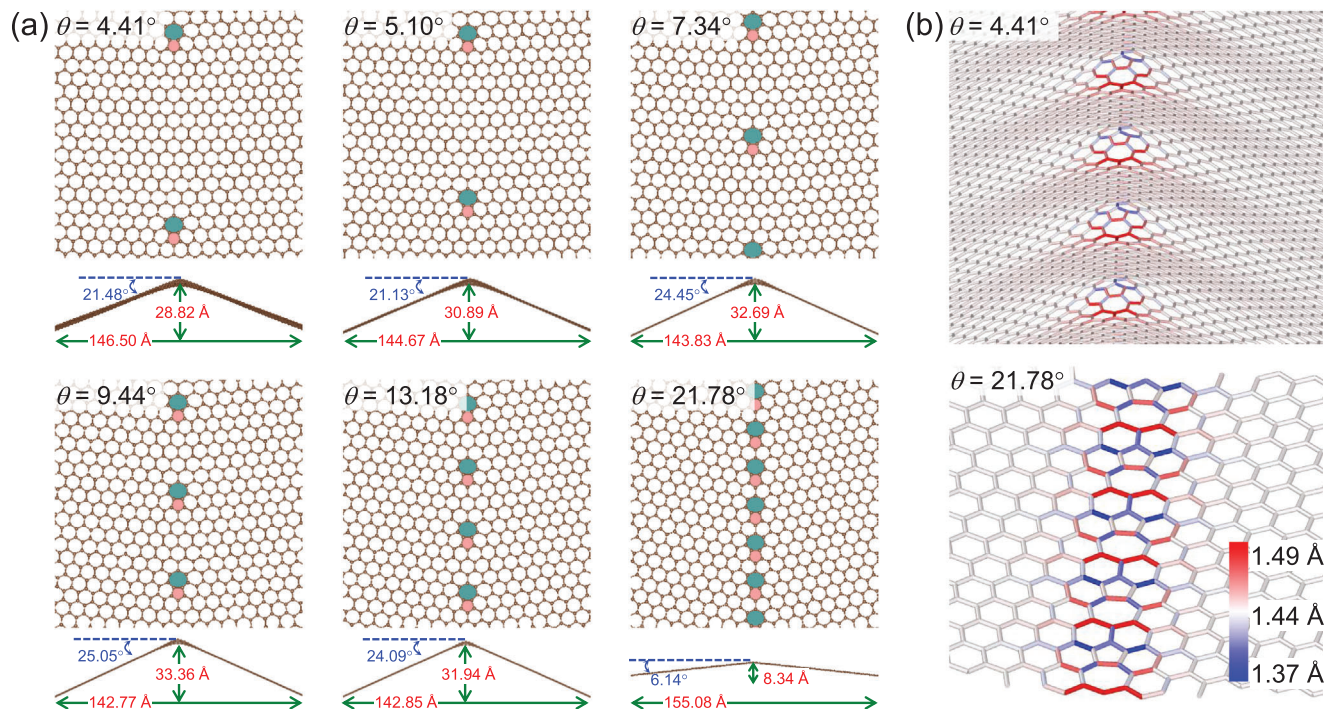
ADVANCED
SCIENCE NEWS
www.advancedsciencenews.com

ADVANCED SCIENCE
Open Access
www.advancedscience.com

Figure 2. a) 6 GBs with different θ (top and side views). b) Bird's eye view along two GB lines. The scale shows bond lengths.

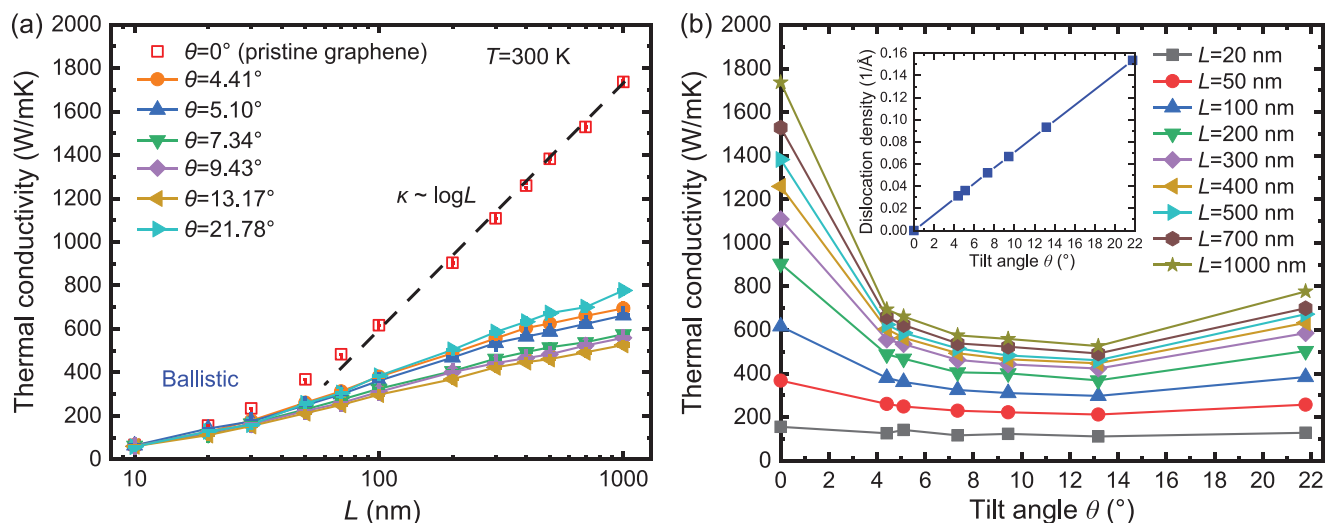**Figure 3.** NEMD computed a) κ_p versus L (semi-log scale) at $T = 300$ K in graphene and along GBs with different θ. b) κ_p versus θ at different L. The inset shows the 5-7 linear density versus θ.

Figure 1a, such as the GB lines extend in all regions. We computed the ballistic transport for $\theta = 4.41°$, $13.18°$ and $21.78°$ and compared them to the pristine graphene. The conductance g is evaluated within the Landauer approach in terms of the frequency (ω) dependent transmission $t_p(\omega)$, as

$$g = \frac{\hbar^2}{2\pi k_B T^2} \int \omega^2 \frac{e^{\frac{\hbar\omega}{k_B T}}}{(e^{\frac{\hbar\omega}{k_B T}} - 1)^2} t_p(\omega) d\omega \qquad (1)$$

Here k_B and $\hbar = h/2\pi$ are the Boltzmann and the reduced Planck constants, respectively. $t_p(\omega)$, in turn, is computed[31,32] based on the dynamical matrix D, as $t_p = Tr[G^r\Gamma_L G^a\Gamma_R]$. The retarded GF is given by $G^r(\omega) = [\omega^2 - D - \Sigma^r_L - \Sigma^r_R]^{-1}$ and $\Gamma_{L,R}$ are the broadening functions, $\Gamma_{L/R} = i[\Sigma^r_{L/R} - \Sigma^a_{L/R}]$, for the "hot" and "cold" contacts.

At $L = 10$ nm considered here, transport is coherent and influenced by the elastic scattering onto the GBs. Plots of $t_p(\omega)$ at different θ are shown in **Figure 4**a. Consistent with NEMD, t_p

**ADVANCED
SCIENCE NEWS**

www.advancedsciencenews.com

**ADVANCED
SCIENCE**
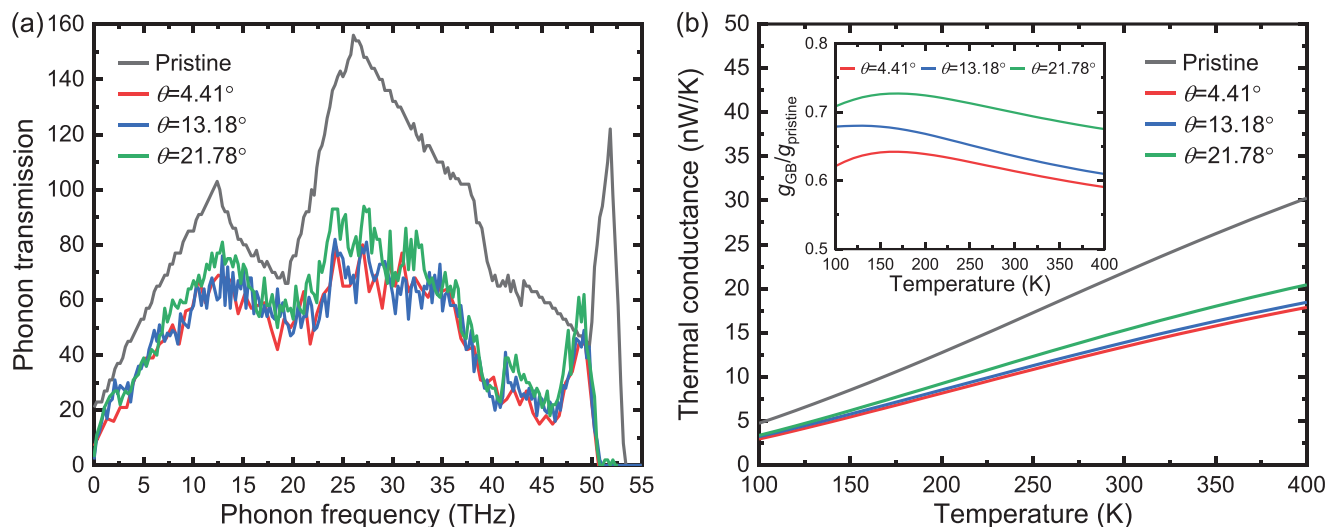Open Access

www.advancedscience.com

Figure 4. GF computed a) phonon transmissions and b) thermal conductances in pristine and along GB graphene. Inset shows GB conductances with respect to graphene.

in pristine graphene is higher than in GBs and yields a higher g value, Figure 4b. The ballistic nature of the conductance is reflected in the integer values of t_p, which depend on the number of phonon states at each ω. Surprisingly, the $t_p(\omega)$ reduction by GBs is inversely proportional to the 5-7 density (i.e., t_p is largest for $\theta = 21.78°$ and smallest for $\theta = 4.41°$). This dependence uncovers the strain field periodicity effect, which operates as a diffraction grating onto the traveling phonons. Through elastic scattering on the strain around the 5-7 cores, reflective diffraction spectra of various orders take place. One one hand, for $\theta = 21.78°$, strain is continuous along the GB line, Figure 2b. Diffraction is dominated by the zero-order recognized by Klemens[7,33] and is associated with a specular reflection and larger group velocity. On the other hand, for $\theta = 4.41°$ GB which has lowest g, the 5-7 defects are ≈ 3.2 nm apart, see Figure S3b, Supporting Information. Destructive interferences introduce stronger phonon localization, which is associated to diffuse reflections and manifests into important thermal resistivity contributions. These important higher diffraction orders are not considered by Klemens.[7,33] This situation reminds of the κ_p reduction along central screw dislocations located in nanowires,[34] an effect also not captured by the classical theory.[7] By introducing periodic nm-scale grooves onto the nanowire surface,[35] κ_p could be further reduced through localization of the phonons that were specularly reflected by the dislocation core.

In summary, the GF calculations obtained that the resistive contributions caused by the diffuse GB reflection scale inversely with the defect density. The g reductions are seen also in the inset of Figure 4b, which shows $g_{GB}/g_{pristine}$ as a function of T, with g_{GB} and $g_{pristine}$ being g for a given GB and graphene pristine, respectively. Remarkably, the $g_{GB}/g_{pristine}$ values of Figure 4b are similar to the ones obtained earlier for transport across GBs.[20] Thus, although the GBs oriented along the T gradient are largely overlooked, we find here that their impact on thermal transport is as substantial as the GBs oriented across the T gradient.

We now focus beyond the pure ballistic regime, where the decay of heat carrying phonons by inelastic scatterings becomes in-

creasingly important. Recalling that in a phonon gas model, thermal conductivity is $\kappa_p = \sum_\lambda c_\lambda v_\lambda^2 \tau_\lambda$, where c_λ, v_λ, and τ_λ are the specific heat capacity, phonon group velocity, and phonon relaxation time of phonon mode λ, respectively. **Figure 5**a shows τ_λ, as calculated by SED scheme[34,36] and room-temperature equilibrium MD runs. When compared to pristine graphene, GBs lead to significant τ_λ reductions. For the "bumpy" GBs, τ_λ decreases with the increase in defect density. This dependence is opposite to the one for the ballistic phonon transmission delineated above, and explains the crossover in κ_p as transport advances into the diffusive regime. However, for $\theta = 21.78°$ GB, where t_p is the largest compared to other GBs, we also find the largest τ_λ in Figure 5(a). This concerted behavior explains the consistently larger κ_p values for $\theta = 21.78°$ GB with respect to the other considered GBs, Figure 3b.

The key role of τ_λ is further supported in Figure 5b by the lattice dynamics[37] computed v_λ, which is another key contributor to κ_p. While for some phonon modes v_λ decreases in $\theta = 21.78°$ GB, it remains unchanged for the acoustic phonon modes, which are playing a main role in thermal conduction. Therefore, the weaker phonon scattering in $\theta = 21.78°$ GB (as reflected by the larger τ_λ) and not an enhancement of v_λ is the mechanism behind the anomalous κ_p behavior. We associate the weaker anharmonic scattering presented in $\theta = 21.78°$ GB to the flatter landscape along the GB line. The 5-7 off-plane distortions at the other θ are enhancing anharmonic scattering as they locally couple the in-plane and out-of-plane degrees of freedom,[20] which are otherwise decoupled.[38]

3. Conclusion

Through the two-dimensionality of the heat transfer, κ_p along linear ultra-narrow GBs is significantly affected. The cause for the κ_p departure from the superdiffusive[39] behavior of pristine graphene and its anomalous dependence on defect density is multifactorial, and it is hidden in the details of the GB structure. κ_p along $\theta = 21.78°$ GB is the largest, which is opposed to the

**ADVANCED
SCIENCE NEWS**

www.advancedsciencenews.com

**ADVANCED
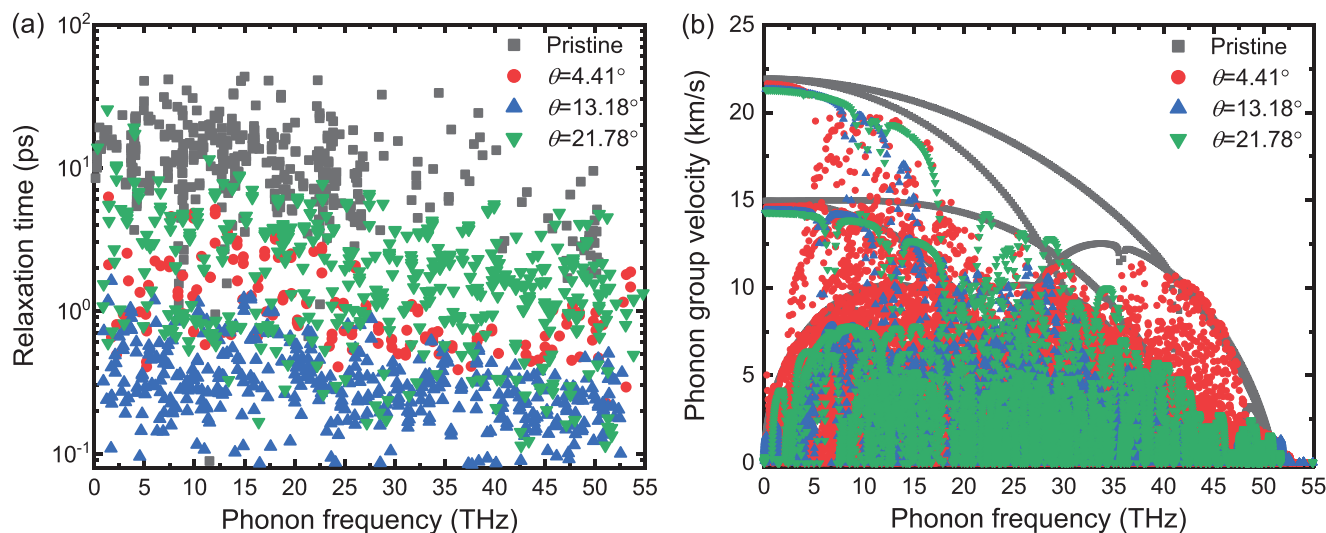SCIENCE**
Open Access

www.advancedscience.com

Figure 5. MD calculated a) phonon relaxation times at $T = 300$ K and b) phonon group velocity in pristine and GB graphene.

expected deterioration of thermal transport at larger dislocation density.[20] The κ_p boost is caused by a diffraction grating effect of the GB strain field periodicity, which leads to a specular scattering, and to a reduced anharmonic scattering associated to the flatter GB landscape. As the 5-7 defects become sparse and "bumpy", elastic scattering on GB becomes diffusive, while anharmonic scattering is enhanced. Even for the case of $\theta = 4.14°$ GB, where the 5-7 defects are ≈3.2 nm apart, the κ_p reduction remains substantial (≈60% for $L = 1000$ nm). This explanation, enabled by state-of-the art atomistic-level NEMD and GF numerical calculations with an accurate accounting for the details of the GB structure, goes beyond the simple phonon specular reflection accounted for by the classical theory of Klemens.[7,33] With thermal transport being vulnerable to GBs, our result can provide guidance for designing GBs that best preserve κ_p.

4. Simulation Section

Structural Relaxations

In preparation for the NEMD and GF calculations, unit cells of the GB structures treated with the optimized Tersoff potential[25] and PBC along x and y directions were subjected to structural relaxations of atomic positions and lattice vectors.

NEMD Simulation

The MD simulations used a time step of 0.5 fs and PBC along the in-plane directions are employed in all NEMD simulations. Prior to the production runs, each configuration of graphene GB was subjected to the following protocol:[40,41] First, NVT simulations with Langevin thermostat[41] were performed for 0.5 ns (1×10^6 steps) to heat up the system to 300 K. Second, NPT simulations[41] were performed for 0.5 ns to release any potential internal stress. Third, NVT simulations[41] were applied for another 0.5 ns to further equilibrate the system. For the production runs, the atoms

at the two sides (the black regions) are fixed to avoid the rotating of ribbons. The adjacent regions labeled with red and blue, are coupled with Langevin thermostats[41] at 310 K and 290 K, respectively. The atoms in the central region are evolved in the NVE ensemble in contact with the adjacent reservoirs. We run another 10 ns (2×10^7 steps) of simulation to construct the linearized temperature gradient and then record the temperature distribution and heat current data.[41] The temperature gradient is obtained by the linear fitting to temperature profiles excluded the regions attached to the heat bath shown in Figure 1b. The heat flux is calculated as the heat rate per unit crossing area of GNRs, which is defined as width multiplied by the inter-layer thickness of graphite.

GF Calculations

Simulations used the atomistic GF method implemented in DFTB+ package.[42] Based on this, a whole system with $L = 10$ nm was divided into left bath, device region, and right bath. The dynamical matrices for each subsystem were obtained within the optimized Tersoff potential[25] description of the interatomic interactions with a finite difference scheme of the atomic forces, not accounting for finite temperature phonon softening effects owing to anharmonicity.

SED Calculations

The SED analysis[43] is employed to obtain the phonon relaxation time. Based on this, the equilibrium MD was carried out to compute the velocity of atoms and then obtained the peaks of SED spectrum for different phonon branches, see Figure S4, Supporting Information. The Lorentzian function fitting technique was employed to determine the phonon relaxation time. SED calculations are performed using an in-house code.

Statistical Analysis

The results in Figure 3 are obtained by averaging results obtained from five individual NEMD trajectories of each GB system. The length (width) of each system L (W) is given in Figure 3 (Figure 2a). Results are represented as means ± SD.

Supporting Information

Supporting Information is available from the Wiley Online Library or from the author.

Conflict of Interest

The authors declare no conflict of interest.

Data Availability Statement

The data that support the findings of this study are available from the corresponding authors upon reasonable request.

[1] E. Pop, *Nano Res.* **2010**, *3*, 147.
[2] A. L. Moore, L. Shi, *Mater. Today* **2014**, *17*, 163.
[3] X. Xu, J. Chen, B. Li, *J. Phys.: Condens. Matter* **2016**, *28*, 483001.
[4] X. Gu, Y. Wei, X. Yin, B. Li, R. Yang, *Rev. Mod. Phys.* **2018**, *90*, 041002.
[5] I. Jo, M. T. Pettes, E. Ou, W. Wu, L. Shi, *Appl. Phys. Lett.* **2014**, *104*, 201902.
[6] Y. Ni, J. Jiang, E. Meletis, T. Dumitrică, *Appl. Phys. Lett.* **2015**, *107*, 031603.
[7] P. G. Klemens, *Proc. Phys. Soc. Sect. A* **1955**, *68*, 1113.
[8] T. Dumitrică, S. Kodambaka, S. Jun, *J. Nanophoton.* **2021**, *6*, 1.
[9] Q. Yu, L. A. Jauregui, W. Wu, R. Colby, J. Tian, Z. Su, H. Cao, Z. Liu, D. Pandey, D. Wei, T. F. Chung, P. Peng, N. P. Guisinger, E. A. Stach, J. Bao, S.-S. Pei, Y. P. Chen, *Nat. Mater.* **2011**, *10*, 443.
[10] P. Y. Huang, C. S. Ruiz-Vargas, A. M. van der Zande, W. S. Whitney, M. P. Levendorf, J. W. Kevek, S. Garg, J. S. Alden, C. J. Hustedt, Y. Zhu, J. Park, P. L. McEuen, D. A. Muller, *Nature* **2011**, *469*, 389.
[11] J. An, E. Voelkl, J. W. Suk, X. Li, C. W. Magnuson, L. Fu, P. Tiemeijer, M. Bischoff, B. Freitag, E. Popova, R. S. Ruoff, *ACS Nano* **2011**, *5*, 2433.
[12] O. V. Yazyev, Y. P. Chen, *Nat. Nanotechnol.* **2014**, *9*, 755.
[13] W. T. Read, W. Shockley, *Phys. Rev.* **1950**, *78*, 275.
[14] H. F. Bettinger, T. Dumitrică, G. E. Scuseria, B. I. Yakobson, *Phys. Rev. B* **2002**, *65*, 041406.
[15] K. Kim, Z. Lee, W. Regan, C. Kisielowski, M. F. Crommie, A. Zettl, *ACS Nano* **2011**, *5*, 2142.
[16] P. Nemes-Incze, P. Vancs, Z. Osvth, G. I. Mrk, X. Jin, Y.-S. Kim, C. Hwang, P. Lambin, C. Chapelier, L. P. Biro, *Carbon* **2013**, *64*, 178.
[17] T.-H. Liu, S.-C. Lee, C.-W. Pao, C.-C. Chang, *Carbon* **2014**, *73*, 432.
[18] A. Fox, U. Ray, T. Li, *J. Appl. Phys.* **2019**, *125*, 015101.
[19] A. Y. Serov, Z.-Y. Ong, E. Pop, *Appl. Phys. Lett.* **2013**, *102*, 033104.
[20] L. M. Sandonas, H. Sevinli, R. Gutierrez, G. Cuniberti, *Adv. Sci.* **2018**, *5*, 1700365.
[21] A. Bagri, S.-P. Kim, R. S. Ruoff, V. B. Shenoy, *Nano Lett.* **2011**, *11*, 3917.
[22] A. Cao, J. Qu, *J. Appl. Phys.* **2012**, *111*, 053529.
[23] K. Azizi, P. Hirvonen, Z. Fan, A. Harju, K. R. Elder, T. Ala-Nissila, S. M. V. Allaei, *Carbon* **2017**, *125*, 384.
[24] S. Plimpton, *J. Comput. Phys.* **1995**, *117*, 1.
[25] L. Lindsay, D. A. Broido, *Phys. Rev. B* **2010**, *81*, 205441.
[26] V. Barone, O. Hod, G. E. Scuseria, *Nano Lett.* **2006**, *6*, 2748.
[27] O. V. Yazyev, S. G. Louie, *Phys. Rev. B* **2010**, *81*, 195420.
[28] F. Banhart, J. Kotakoski, A. V. Krasheninnikov, *ACS Nano* **2011**, *5*, 26.
[29] S. Ghosh, I. Calizo, D. Teweldebrhan, E. P. Pokatilov, D. L. Nika, A. A. Balandin, W. Bao, F. Miao, C. N. Lau, *Appl. Phys. Lett.* **2008**, *92*, 151911.
[30] X. Xu, L. F. C. Pereira, Y. Wang, J. Wu, K. Zhang, W. Zhao, S. Bae, C. Tinh Bui, R. Xie, J. T. L. Thong, B. H. Hong, K. P. Loh, D. Donadio, B. Li, B. Özyilmaz, *Nat. Commun.* **2014**, *5*, 3689.
[31] L. Medrano Sandonas, D. Teich, R. Gutierrez, T. Lorenz, A. Pecchia, G. Seifert, G. Cuniberti, *J. Phys. Chem. C* **2016**, *120*, 18841.
[32] L. M. Sandonas, R. Gutierrez, A. Pecchia, A. Croy, G. Cuniberti, *Entropy* **2019**, *21*, 735.
[33] M. Omini, A. Sparavigna, *Phys. Rev. B* **2000**, *61*, 6677.
[34] Y. Ni, S. Xiong, S. Volz, T. Dumitrică, *Phys. Rev. Lett.* **2014**, *113*, 124301.
[35] J. Al-Ghalith, Y. Ni, T. Dumitrică, *Phys. Chem. Chem. Phys.* **2016**, *18*, 9888.
[36] J. A. Thomas, J. E. Turney, R. M. Iutzi, C. H. Amon, A. J. H. McGaughey, *Phys. Rev. B* **2010**, *81*, 081411(R).
[37] J. D. Gale, A. L. Rohl, *Mol. Simul.* **2003**, *29*, 291.
[38] I. Nikiforov, E. Dontsova, R. D. James, T. Dumitrică, *Phys. Rev. B* **2014**, *89*, 155437.
[39] S.-N. Li, B.-Y. Cao, *Appl. Math. Lett.* **2020**, *99*, 105992.
[40] J. Zhang, Y. Hong, Z. Tong, Z. Xiao, H. Bao, Y. Yue, *Phys. Chem. Chem. Phys.* **2015**, *17*, 23704.
[41] H. Wei, H. Bao, X. Ruan, *Nano Energy* **2020**, *71*, 104619.
[42] B. Hourahine, B. Aradi, V. Blum, F. Bonafé, A. Buccheri, C. Camacho, C. Cevallos, M. Y. Deshaye, T. Dumitrică, A. Dominguez, S. Ehlert, M. Elstner, T. van der Heide, J. Hermann, S. Irle, J. J. Kranz, C. Köuhler, T. Kowalczyk, T. Kubař, I. S. Lee, V. Lutsker, R. J. Maurer, S. K. Min, I. Mitchell, C. Negre, T. A. Niehaus, A. M. N. Niklasson, A. J. Page, A. Pecchia, G. Penazzi, et al., *J. Chem. Phys.* **2020**, *152*, 124101.
[43] B. Qiu, H. Bao, G. Zhang, Y. Wu, X. Ruan, *Comput. Mater. Sci.* **2012**, *53*, 278.